

Improved Lattice Spectroscopy of Minimal Walking Technicolor

Francis Bursa

Jesus College, University of Cambridge, Cambridge, England

E-mail: f.bursa@damtp.cam.ac.uk

Luigi Del Debbio

SUPA, School of Physics and Astronomy, University of Edinburgh, Edinburgh, Scotland

E-mail: luigi.del.debbio@ed.ac.uk

David Henty

EPCC, University of Edinburgh, Edinburgh, Scotland

E-mail: d.henty@epcc.ed.ac.uk

Eoin Kerrane

SUPA, School of Physics and Astronomy, University of Edinburgh, Edinburgh, Scotland

E-mail: eoin.kerrane@ed.ac.uk

Biagio Lucini

College of Science, Swansea University, Swansea, Wales

E-mail: b.lucini@swansea.ac.uk

Agostino Patella

CERN, Geneva, Switzerland

E-mail: agostino.patella@cern.ch

Claudio Pica

CP³-Origins & IMADA, University of Southern Denmark, Odense, Denmark

E-mail: pica@cp3.sdu.dk

Thomas Pickup

Rudolf Peierls Centre for Theoretical Physics, University of Oxford, Oxford, England

E-mail: pickup@thphys.ox.ac.uk

Antonio Rago

Department of Physics, Bergische Universität Wuppertal, Wuppertal, Germany

E-mail: rago@physik.uni-wuppertal.de

Abstract

We present a numerical study of spectroscopic observables in the $SU(2)$ gauge theory with two adjoint fermions using improved source and sink operators. We compare in detail our improved results with previous determinations of masses that used point sources and sinks and we investigate possible systematic effects in both cases. Such comparison enables us to clearly assess the impact of a short temporal extent on the physical picture, and to investigate some effects due to the finite spatial box. While confirming the IR-conformal behaviour of the theory, our investigation shows that in order to make firm quantitative predictions, a better handle on finite size effects is needed.

1 Introduction

A new strongly interacting theory [1, 2] with an approximate [3, 4, 5] or exact [6] infra-red (IR) fixed point is an appealing possibility for explaining electroweak symmetry breaking. This framework, known as Technicolor, has been reviewed recently in e.g. [7, 8, 9]. Technicolor theories are inherently non-perturbative and therefore require adequate tools to study their strong dynamics. Theories with conformal or near-conformal dynamics can be exposed in the context of the gauge-string duality [10, 11]. However, in addition to the wanted fermion and gauge boson degrees of freedom, field theory duals of string theories in general contain extra scalar fields. A possible *ab initio* approach relies on numerical simulations of candidate Technicolor theories discretised on a spacetime lattice (see e.g. [12, 13] for recent reviews).

One could generate an infra-red fixed point in a gauge theory by adding a low number of fermion flavours in higher gauge representations to a gauge theory with a low number of colours. The minimal vector-like gauge theory with this property, termed minimal walking technicolor (MWT), has gauge group $SU(2)$ and two flavours of Dirac fermions in the adjoint representation [14]. Some recent lattice studies of MWT [15, 16, 17] have attempted to identify a near-conformal behaviour directly from the behaviour of the coupling and anomalous dimensions of the theory under RG flow. Others, including this work, perform measurements of physical observables in the theory and attempt to identify signals of near-conformal dynamics from their behaviour [18, 19, 20, 21, 22, 23, 24, 25]. All the evidence accumulated so far for this theory favours a conformal or near-conformal scenario and seems to exclude standard confinement and chiral symmetry breaking behaviour. However, more systematic studies need to be performed before the IR properties of the theory can be determined with confidence.

MWT with a non-zero fermion mass and defined in a finite volume, as simulated for practical reasons on the lattice, cannot be conformal. If the chiral continuum theory possesses an infra-red fixed point, the lattice results will be described by a mass-deformed conformal gauge theory [26, 22, 27, 25, 24, 28, 29]. In approaching a conformal limit, the theory respects the hyperscaling property, whereby all spectral masses M in the theory scale identically. They must vanish in the limit of vanishing fermion mass m . If the IR fixed point is approximate, the theory displays conformal behaviour for an intermediate range of masses m and crosses over to the confining and chiral symmetry breaking behaviour in the chiral limit.

The standard way to extract masses from lattice simulations is to look at the exponential decay of correlators of operators with the quantum numbers of interest. For infinite separation between the source and sink operator, the exponential decay is governed by the ground state mass in the channel being explored. At finite time extent, this leading behaviour receives corrections that are exponentially suppressed in the mass difference between the ground state and the excitations. Underestimating the importance of these corrections leads to systematic errors in the determination of the ground state mass. In addition to the effects of the finite maximal separation between the source and the sink (often referred to as finite temperature effects), the finite spatial extension of the lattice can also give sizeable corrections to the spectral masses.

The simplest source and sink observables to study for mesons are fermion bilinears in which the two fermion fields are at the same lattice point (*point sources*). These sources

have been widely used in previous investigations of the spectrum of MWT. However, the experience accumulated over 30 years of numerical studies in lattice QCD favours the use of *extended sources*, which are gauge-invariant combinations of two fermion fields at different points, engineered for reducing the contamination from the excited states. In lattice QCD masses extracted from correlators of extended sources prove to be affected by smaller systematic errors. In this paper, we investigate whether this proves to be the case also for MWT. Specifically, we perform a study of mesonic observables extracted from extended sources using the configurations presented in [19, 22, 25]. We explore a large set of schemes for building extended operators and we systematically analyse their efficiency for the computation of meson masses and decay constants, comparing the results with results obtained using point sources. With this study, we expect to determine the size of systematic uncertainties in current studies, which have as yet been largely unexplored, and to assess their impact on the physical picture emerging from the previous spectroscopical studies. Some of the results presented here have already appeared in Ref. [30].

The rest of the paper is organised as follows. In Sec. 2 we describe the background to this study and briefly illustrate the effects of the use of different smearings on effective observables. Technical details on the smearing procedures and the resulting observables can be found in Appendices A and B respectively. In Sec. 3 we quantify the consequences of the smearing both for autocorrelation times and quality of plateaux. A full set of results obtained using wall smearing are presented in Sec. 4, while in Sec. 5 we comment on the significant finite-volume effects highlighted by the smeared results. Appendices C and D list the numerical values of the quantities studied in this work. Finally, our conclusions are reported in Sect. 6.

2 Systematic Spectroscopy

This study builds on the work described in [19, 25] where spectroscopic observables of MWT were measured through lattice simulations. The computation was performed using the *HiRep* code, designed to simulate theories of generic number of colours, and with fermions in a generic representation of the gauge group. The simulations used the Wilson gauge action, and the Wilson fermion formulation along with the RHMC algorithm. A number of lattice volumes have been analysed, from 16×8^3 to 64×24^3 with a range of bare quark masses. The majority of the ensembles have been generated at $\beta = 2.25$, although we do here present the results of some additional runs on the largest lattice at $\beta = 2.1$.

For this study we have performed some alternative analyses to those in [25]. The *Chroma* suite of lattice software [31] has been extended to operate with several fermionic representations other than the fundamental, including the adjoint. This will allow us to utilise the in-built smearing routines of *Chroma* for our spectroscopic study.

In order to test the modified *Chroma*, we measured the local correlators as defined in (A.3), with $\Gamma = \Gamma'$ both with *HiRep* ($f_{\Gamma}^{(h)}(t)$) and *Chroma* ($f_{\Gamma}^{(c)}(t)$). We used an ensemble of configurations on a 8×4^3 lattice with $\beta = 2.25$ and fermion bare mass $am_0 = -1$.

Fig. 1 illustrates the discrepancy between the two determinations, defined as:

$$D_1 = \sqrt{\sum_t \left(f_\Gamma^{(c)}(t) - f_\Gamma^{(h)}(t) \right)^2} \quad D_2 = \sqrt{\sum_t \left(\frac{f_\Gamma^{(c)}(t) - f_\Gamma^{(h)}(t)}{f_\Gamma^{(h)}(t)} \right)^2}. \quad (2.1)$$

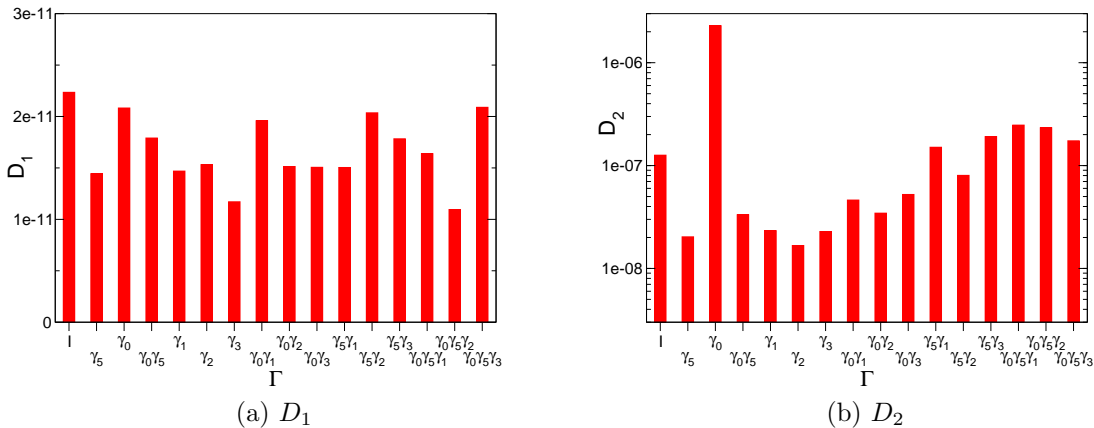


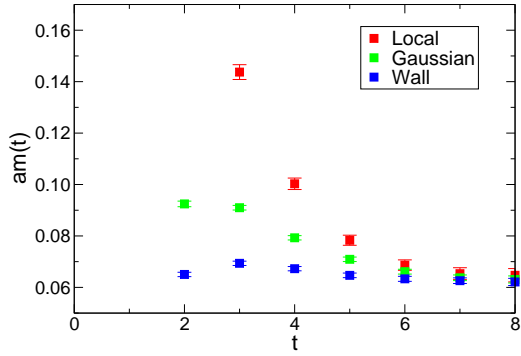
Figure 1: Discrepancies between local correlators from *HiRep* and *Chroma*, computed to test the extension of *Chroma* (for working with adjoint fermions) against HiRep.

We proceeded to utilise the in-built smearing routines found in *Chroma* to perform measurements on the gauge configurations generated with *HiRep* using a number of different quark smearings. We have investigated the use of both wall-smearing and a gauge invariant gaussian smearing, as defined in App. A.2. Definitions of all observables discussed can be found in App. B.

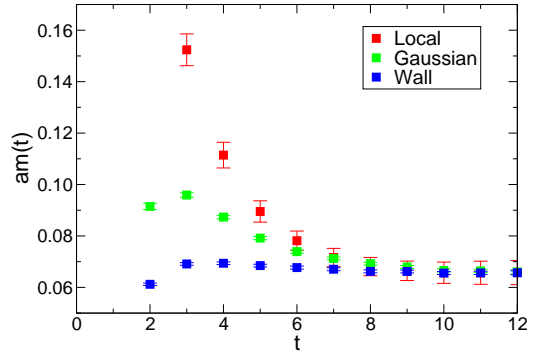
Gaussian smearing involves two parameters, which can be chosen to optimize the technique. They are the width of the smearing function and the number of applications of the smearing operator, which must be large enough to reasonably approximate the gaussian form. These two parameters have been adjusted in order to maximize the overlap of the smeared operator with the ground state. On the other hand, the wall-smearing is a parameter-free procedure.

We systematically compared local, gaussian (with optimised parameters) and wall-smearred sources on our ensembles. At our lightest masses, the wall-smearred sources have the largest overlap with the ground state, which is reflected in the flattest effective masses. In Figs. 2, 3, 4 we show respectively the PCAC and PS effective masses and the PS effective decay constant computed with the three methods.

Since we are mainly interested in the light masses, we will focus on the wall-smearred results in the rest of this work.

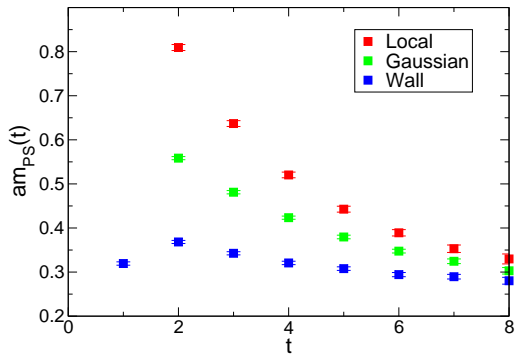


(a) 16×8^3

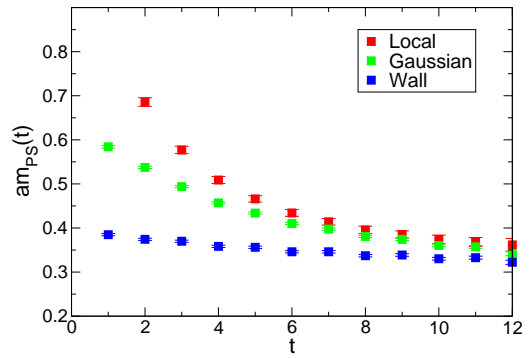


(b) 24×12^3

Figure 2: Comparison of the PCAC mass from different smearings at $am_0 = -1.175$.



(a) 16×8^3



(b) 24×12^3

Figure 3: Comparison of the pseudoscalar mass from different smearings at $am_0 = -1.175$.

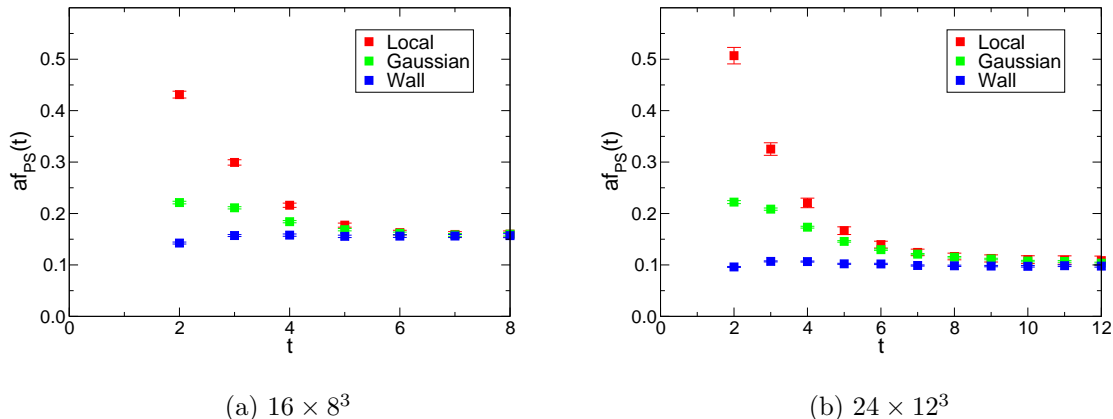


Figure 4: Comparison of the pseudoscalar decay constant from different smearings at $am_0 = -1.175$.

3 Effectiveness of the wall-smearred sources

Using smeared sources allows us to choose an operator with a larger projection onto the ground state of a given channel. The wave-function of the ground state is spread over many lattice sites, and we can improve the overlap of the operator with the ground state by giving a spatial size to the source. The smeared correlator will be less contaminated by the excited states, and therefore it will be characterized by a single cosh signal for a larger temporal separation than the one constructed with point operators. This is reflected in a longer plateau in the effective mass. On the contrary one drawback of using smeared sources is that it makes the analysis more sensitive to the algorithm's autocorrelation time. In this section we propose a quantitative study of these two aspects: the behaviour of the size of the plateaux for different kinds of sources, and the autocorrelation time connected with the use of these sources.

3.1 Autocorrelations

Correlators generated using sources with an extended spatial profile are expected to be associated with longer autocorrelation times, due to the fact that the low energy modes of the fields need more Monte-Carlo time to propagate. This effect is observed throughout our study, indeed the autocorrelation time associated with the results from smeared correlators is generically at least of the order of twice that of those involved with the local correlators. This is supported both by the direct measurement of the integrated autocorrelation time [32] associated with the observables, and by the analysis of the behaviour of the standard deviation of the observables.

Both the aforementioned studies have been performed by grouping the N data into N/b blocks of a given length b . A reduced dataset of length N/b is created by averaging the required statistic over each block. A bootstrap analysis is then performed on the reduced dataset. By increasing the block size b , we are creating effective estimates less and less autocorrelated, hence when the block size is bigger than the autocorrelation we

expect to see a plateau appearing in the standard deviation, signaling that the reduced dataset is decorrelated. We observe that the plateau starts at a block size corresponding to an integrated autocorrelation time of order 1.

Our analysis of the autocorrelation is illustrated in Fig. 5, for the PS effective mass obtained with both local (L), and wall-smearred (W) sources, evaluated at two temporal points.

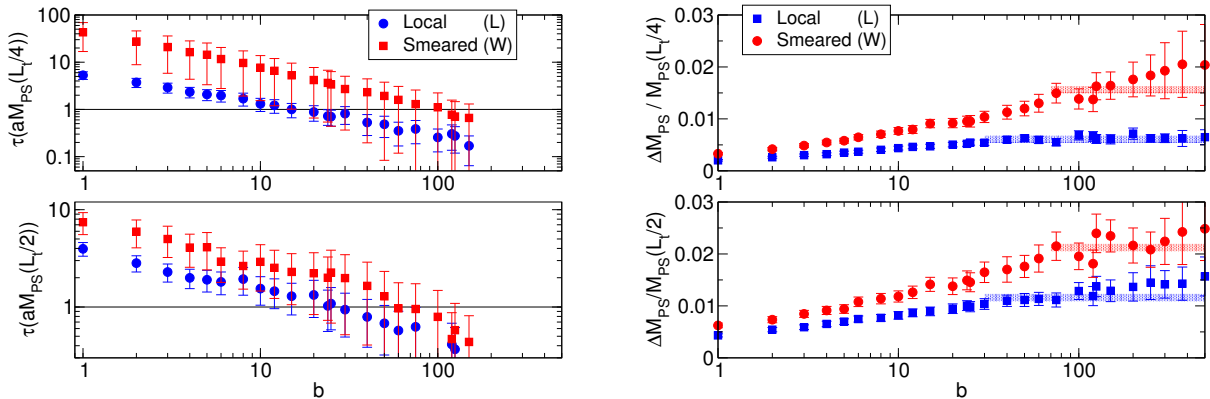


Figure 5: Autocorrelation analysis conducted on a 24×12^3 lattice at $am_0 = -1.175$, for the PS effective mass in two temporal points. In the left panel, integrated autocorrelation time as a function of the block size b . In the right panel, relative error as a function of the block size b . The plateaux of the relative error are highlighted with shadowed rectangles. The plateaux in the relative error set in when the integrated autocorrelation time becomes of order 1.

From the left panel of Fig. 5 we see that the measured autocorrelation time for the smearred results are generically larger than those for the local results. From the right panel of Fig. 5 we see that the standard deviation of our observable increases for both sets of correlators as we increase the block size from zero, up to a point where it appears to reach a plateau for a significant range of b for both cases. The value of b where this plateau sets in is interpreted as the length in simulation time over which the data are uncorrelated. From the right panel of Fig. 5 we would conclude that the autocorrelation time of our local result was ~ 30 while that of the smearred result was ~ 80 . Indeed returning to the left panel of Fig. 5 we see that at this value of b , the corresponding value of the integrated autocorrelation time is close to 1, which supports our conclusion.

This picture is replicated across our ensembles, and we have accounted for this in our results by conducting our bootstrap analysis over appropriately reduced datasets.

3.2 Plateaux of the effective masses

If the smearing procedure is effectively suppressing the contribution of the excited states to the correlators, one has to observe the effective masses flattening around the midpoint $t = L_t/2$, and the plateaux becoming longer when visible. We can quantitatively estimate the flatness of the effective mass using the absolute value of the incremental ratio of the effective mass between $t = L_t/2$ and $t = L_t/2 - \Delta t$:

$$\frac{\Delta m_{PS}}{\Delta t} \equiv \left| \frac{m_{PS}(L_t/2 - \Delta t) - m_{PS}(L_t/2)}{\Delta t} \right|. \quad (3.1)$$

A value for $\Delta m_{PS}/\Delta t$ compatible with zero implies that the plateau in the effective mass is long at least Δt points. For very small values of Δt the incremental ratio is dominated by the statistical error. On the other hand the effective masses obtained with smeared sources are sometimes non monotonic. In this case the incremental ratio defined with a too large value for Δt is not a good estimate for the flatness of the plateau. An intermediate range of values for Δt exists, in which our analysis makes sense. We explicitly checked that our conclusions do not change choosing Δt in such a range, and we chose $\Delta t = 4$ for definiteness.

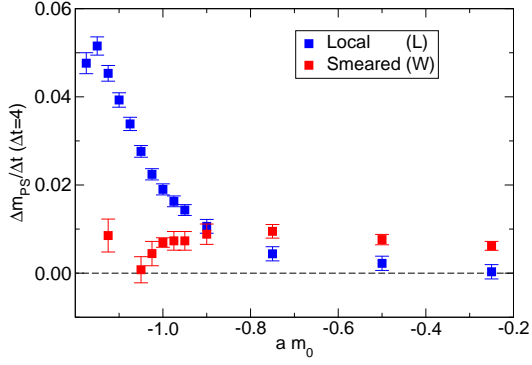
In general the smaller $\Delta m_{PS}/\Delta t$ is, the flatter the plateau. Notice that it is important to take the absolute value in the definition above: while the effective mass defined from local correlators is always decreasing, it is not so for smeared correlators.

In Fig. 6, the quantity $\Delta m_{PS}/\Delta t$ is plotted for all our pseudoscalar effective masses on the 16×8^3 , 24×12^3 and 32×16^3 lattices, both for local and wall-smeared correlators.

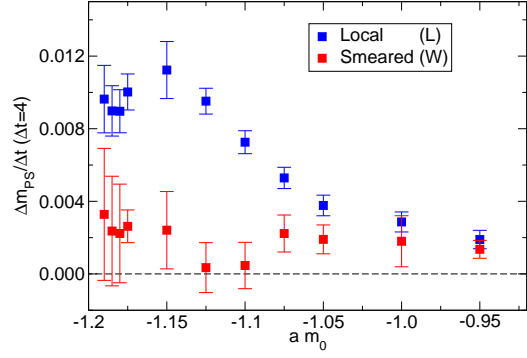
One expects that at small masses the wave function of the pseudoscalar meson is more spread, hence the wall-smeared source should have a larger overlap with the ground state. On the contrary at large masses the wave function is more localised therefore the local sources should work better. Our analysis presented in Fig. 6 substantiates this expectation. On the 16×8^3 lattice the wall-smeared sources give better or comparable plateaux than the local sources for masses $am_0 \leq -0.9$. On the 24×12^3 and 32×16^3 lattices the wall-smeared sources are to be (sometimes marginally) preferred to the local ones for all the simulated masses.

In the presentation of the results obtained from wall-smeared sources we will always cut the masses in the 16×8^3 lattice for which the local sources are actually preferable to the wall-smeared ones, unless otherwise stated.

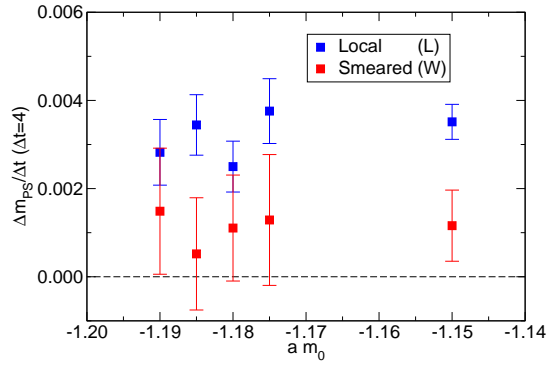
Finally, we point out that the same analyses using the effective V meson mass and the effective PS decay constant produce very similar results.



(a) 16×8^3



(b) 24×12^3



(c) 32×16^3

Figure 6: Incremental ratio $\Delta m_{PS}/\Delta t$ as a function of the bare mass. The smaller this quantity, the better the quality of the plateau of the PS effective mass. On the 16×8^3 lattice, the local correlators give flatter plateaux for bare masses larger than -0.8 , while the smearing is effective below -0.9 . On the 24×12^3 lattice, the local and smeared sources give plateaux of similar quality for the two heaviest masses, while the smearing is effective for all the other masses. Finally the smearing is always effective on the 32×16^3 .

4 Results

In the present section, we will present our results for the mesonic observables from the wall-smearred sources. Complete results of all observables analysed are also presented in Sec. C. Although only the results at $\beta = 2.25$ will be discussed in detail, measurements at $\beta = 2.1$ can also be found in the tables. For the full local results, the reader is referred to [25].

We will consider only those fermionic masses for which the wall-smearred sources give an improvement on the plateaux of the effective masses with respect to the local sources, as discussed in Sec. 3.2. For all these masses, the wall-smearred results have to be trusted more than the local ones. The disagreement between the two determinations gives an estimate of the systematic error due to a bad determination of the plateaux, mainly affecting our previous results obtained from the local sources.

In order to quantify this disagreement we use two different estimators: the *pull* and the *relative discrepancy*. We will denote $O_L \pm \Delta O_L$ and $O_S \pm \Delta O_S$ the determination of the generic observable O using respectively local and smearred sources. The pull estimates the relative size of the systematic and statistical errors and is defined as:

$$P(O) = \frac{|O_L - O_S|}{\sqrt{\Delta O_L^2 + \Delta O_S^2}}. \quad (4.1)$$

A small value for the pull is desirable, indicating that the systematic errors are smaller than the statistical ones. However a small value for the pull can be obtained either with a small systematic error or with a large statistical one. Therefore it is not an absolute estimator of the goodness of a measurement. The relative discrepancy estimates the systematic error, relative to the average of the two determinations:

$$D(O) = \frac{2|O_L - O_S|}{O_L + O_S}. \quad (4.2)$$

A small value for the relative discrepancy indicates that the systematic effects contribute to a small fraction of the determination of the observable O .

In what follows, we will consider separately the PCAC quark mass, the PS and V masses and their ratios, the PS and V decay constant. Again, we refer the reader to Appendix B for the definition of these observables. We will present the results for the wall-smearing sources, and we will discuss the differences with the local-source results using the pull and the relative discrepancy.

4.1 PCAC mass

In Fig. 7 results for the PCAC mass from the wall-smearred correlators on all $\beta = 2.25$ ensembles are presented. The inset illustrates a close up of the approach to the chiral limit, with a linear extrapolation to zero quark mass. Using this we find the critical bare quark mass to be $am_c = -1.2022(14)$, from a fit using the three lightest points on the 24×12^3 lattice, which compares very well to the result obtained from the local data [25].

In Fig. 8 we show the stability of this fit against varying the number of points used. We compare this to the result obtained from local correlators, noting the agreement. It

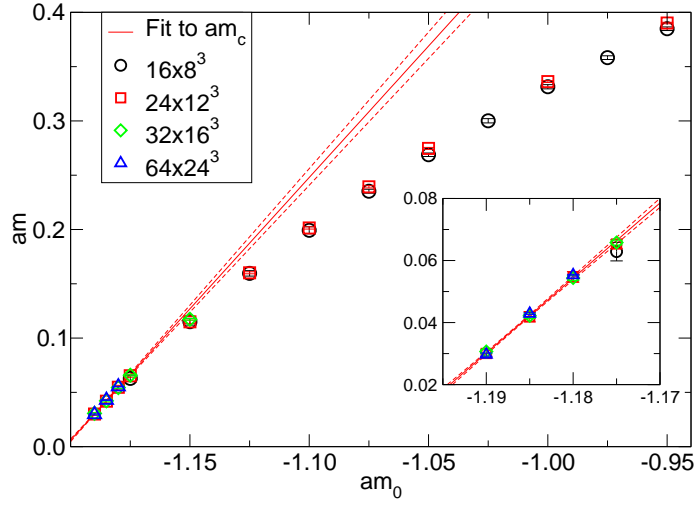


Figure 7: PCAC quark mass for ensembles at $\beta = 2.25$, computed with wall-smeared sources, as a function of the quark bare mass. The result of the linear fit for extracting the critical bare mass is also shown. In the inset, the lightest masses are zoomed in.

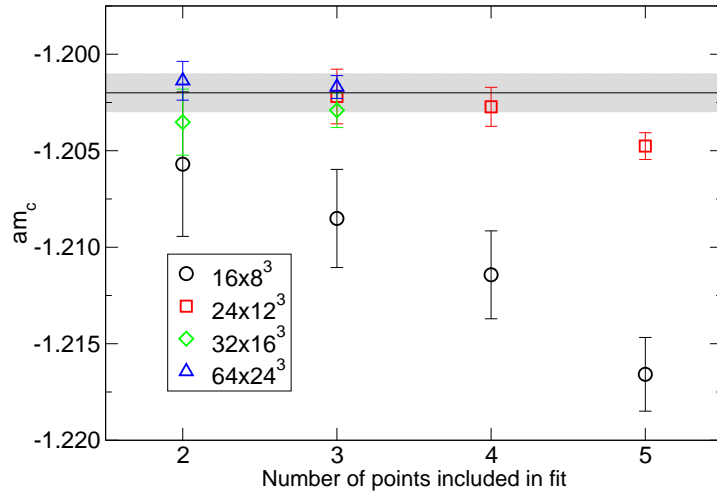


Figure 8: Critical quark mass extracted from a linear fit with different fit ranges. The critical mass as obtained from local data is shown as a grey band.

is also clear that finite volume effects for this quantity are at most comparable with the statistical uncertainty.

In Fig. 9 we show the pull and the relative discrepancy as defined in Eqs. (4.1) and (4.2) between the local and wall-smearred determinations of the PCAC quark mass. We include all the masses at which the wall-smearred sources give an improvement of the plateaux in the effective masses over the local sources. As shown in the left panel of Fig. 9, the pull is always smaller than 1 (or marginally larger than 1 for the smallest volume), indicating that the systematic error due to a short temporal direction is of the order of the statistical uncertainty. The right panel of Fig. 9 shows that the systematic error is of order of a few percents for the PCAC mass.

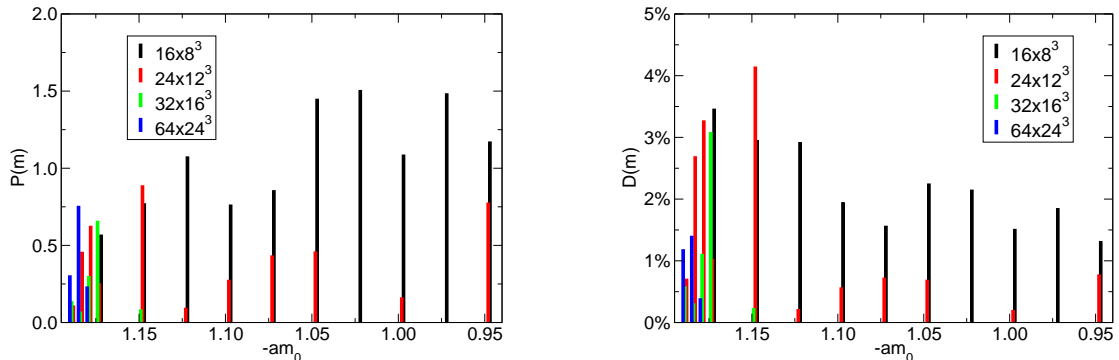


Figure 9: Pull and relative discrepancy as defined in Eqs. (4.1) and (4.2) for the PCAC quark mass ($\beta = 2.25$).

4.2 Meson masses

Fig. 10 shows the results obtained for the pseudoscalar mass M_{PS} as a function of the PCAC quark mass m , from the $\beta = 2.25$ data. Fig. 11 shows the ratio M_V/M_{PS} . We recall that the existence of a plateau at small masses of this ratio was one of the main ingredients for arguing in favour of an IR fixed point in [22] and [25]. We notice that the smeared results stabilize the plateaux at very small masses (especially by smoothing the behaviour of the largest volumes), while making more visible some finite-volume effects at intermediate masses. We will discuss the finite-volume effects in Sec. 5.

We also report the pull and relative discrepancy as defined in Eqs. (4.1) and (4.2) between the local and wall-smearred determinations of the PS mass in Fig. 12. Again, we include all the masses at which the wall-smearred sources give an improvement of the plateaux in the effective masses over the local sources. The local and smeared sources give quite different results at small masses. The relative discrepancy has a very regular behaviour: it is larger for lighter masses or smaller volumes. For bare masses below -1.15 one has to use lattices larger than the 24×12^3 in order to keep the relative discrepancy below the 10% level. Although the relative discrepancy can get fairly large at these masses, the pull is always below 3 which means that the two determinations are

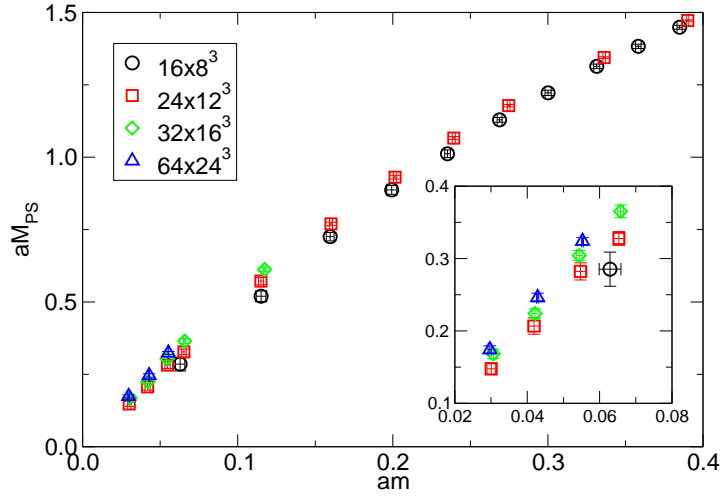


Figure 10: Pseudoscalar meson mass for ensembles at $\beta = 2.25$, computed with wall-smearred sources, as a function of the PCAC mass. In the inset, the lightest masses are zoomed in.

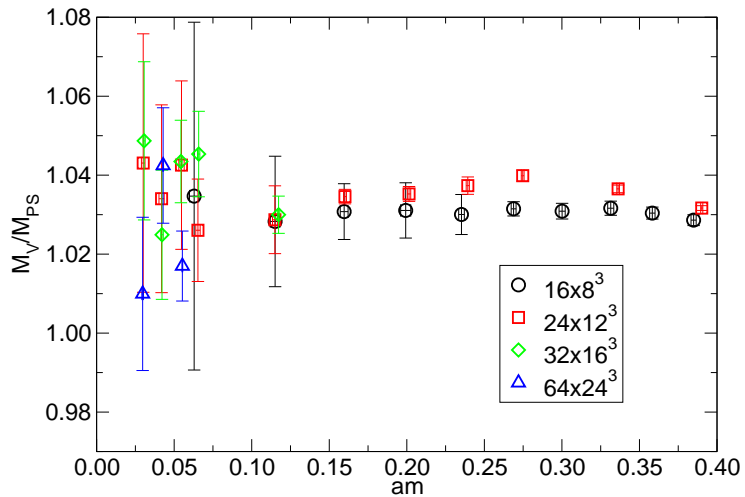


Figure 11: Ratio of M_V to M_{PS} for ensembles at $\beta = 2.25$, computed with wall-smearred sources, as a function of the PCAC mass. The plateau in this ratio at small masses has been interpreted in our previous works [22, 25] as a signal for IR-conformality. The smeared sources have amplified the finite volume effects at masses around $am \simeq 0.3$. This effect will be discussed in Sec. 5

compatible within the 3σ range. This effect is generated by an increase of the relative statistical error at light masses.

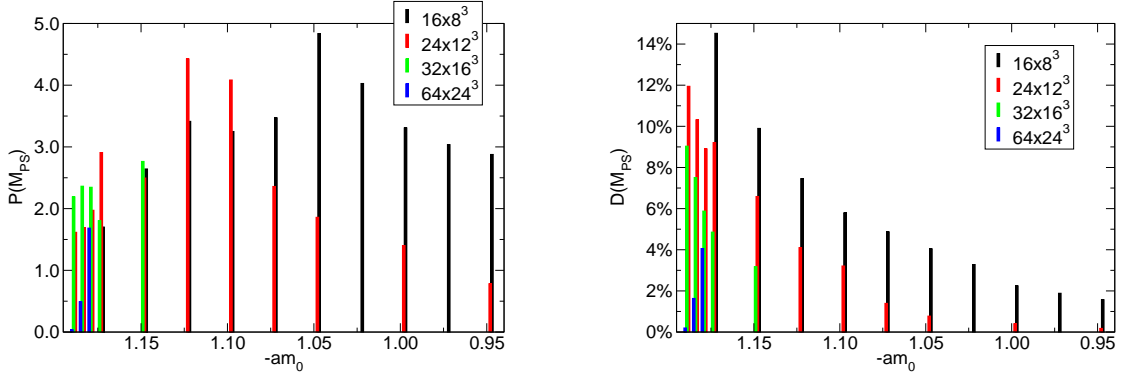


Figure 12: Pull and relative discrepancy as defined in Eqs. (4.1) and (4.2) for the PS mass ($\beta = 2.25$).

Fig. 13 shows the pull and relative discrepancy between the local and wall-smearred determinations of the M_V/M_{PS} ratio. The situation is better here. The central values of the two determinations never differ by more than 5% (relative discrepancy), and they are generally compatible (except the smallest volume) within the 2σ range (pull).

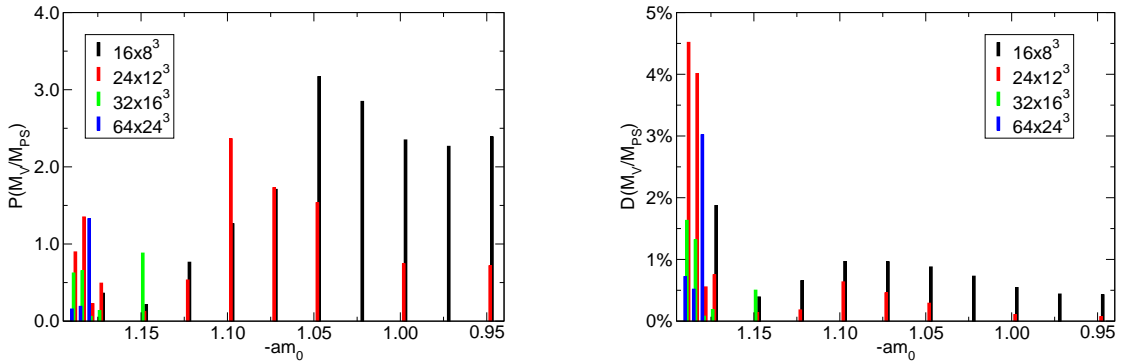


Figure 13: Pull and relative discrepancy as defined in Eqs. (4.1) and (4.2) for the ratio of the V mass over the PS mass ($\beta = 2.25$).

4.3 Decay constants

Among the observables considered in this study, the PS decay constant is the quantity most affected by systematic errors due to a short temporal dimension. The relative discrepancy between the local and smeared determinations (Fig. 14) is almost always very large. On the 24×12^3 , 32×16^3 and 64×24^3 lattices, this large relative discrepancy is partly

compensated by a large statistical error. In most of the cases the two determinations are compatible (sometimes marginally) within 3σ of the statistical uncertainty (pull). On the 16×8^3 lattice, the difference is more dramatic. However for intermediate masses, the wall-smearred source gives a better defined plateau in the effective PS decay constant as discussed in Sec. 3.2, and therefore the smeared results have to be trusted more than the local ones.

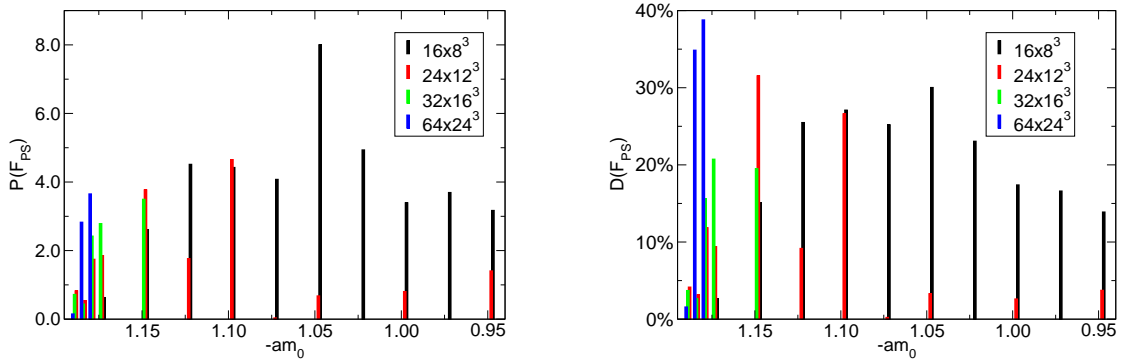


Figure 14: Pull and relative discrepancy as defined in Eqs. (4.1) and (4.2) for the PS decay constant ($\beta = 2.25$).

Fig. 15 shows the results for the PS decay constant from wall-smearred sources. The difference between the results on the 16×8^3 and 24×12^3 lattices are striking (and was absent in the local determination). This finite-volume effect will be discussed in Sec. 5. We also show for completeness the ratio F_V/F_{PS} in Fig. 16.

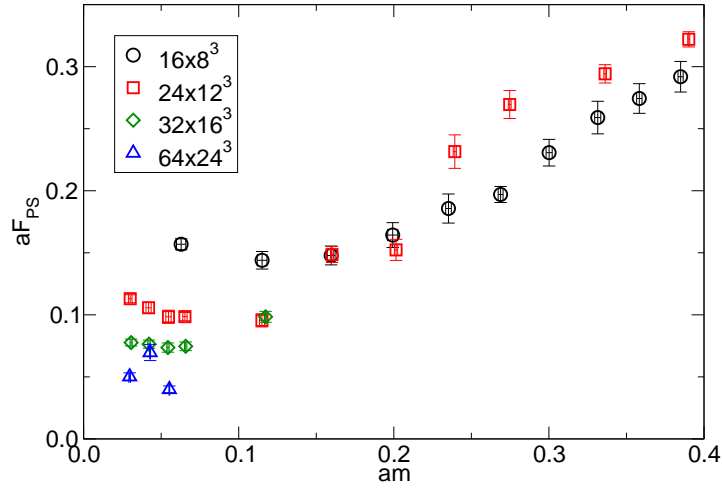


Figure 15: Pseudoscalar decay constant for ensembles at $\beta = 2.25$, computed with wall-smearred sources, as a function of the PCAC mass.

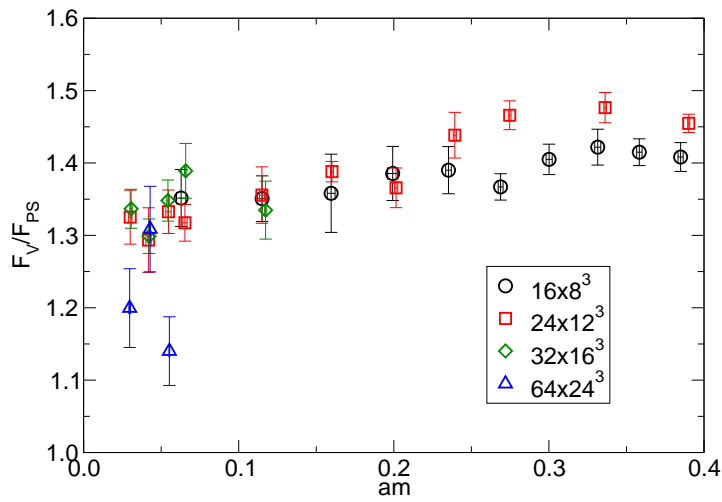


Figure 16: Ratio of vector and pseudoscalar decay constants.

5 Comments on finite-volume effects

The wall-smearred results helped us to better understand how finite spatial volume affects the mesonic observables. In Fig. 17 we plot the PS and V masses, their ratio and PS decay constant on the 16×8^3 and 24×12^3 lattices for $am_0 = -1.05$ and $\beta = 2.25$, both from local and wall-smearred sources. For each observable, the gap between the two lattices becomes wider when wall-smearred sources are considered. Having only the data from local sources, one can be tempted to underestimate the finite-volume errors. This would be a mistake: the mild dependence on the volume of the local data is actually given by a cancellation of two larger effects: the finite volume and the bad determination of the plateaux in the effective masses.

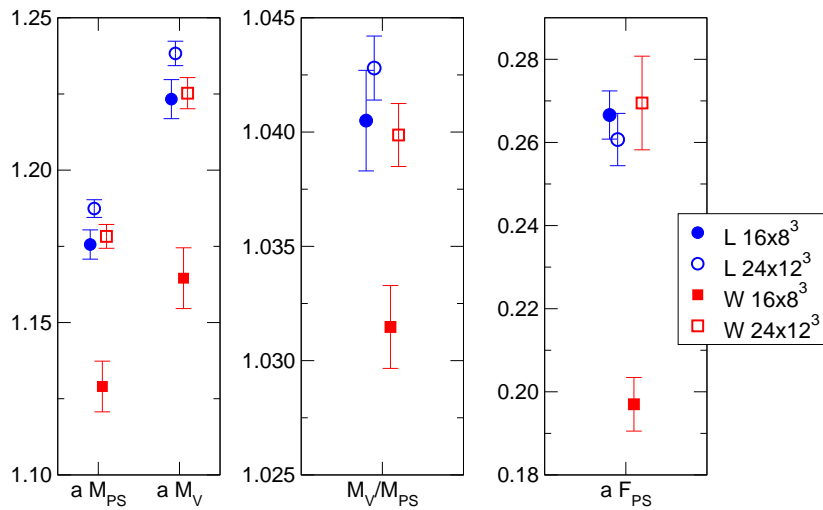


Figure 17: PS and V masses, their ratio and PS decay constant on 16×8^3 and 24×12^3 lattices for $am_0 = -1.05$ and $\beta = 2.25$ (L=local, W=wall).

In order to clarify this point, it is useful to look directly at the effective PS mass (Fig. 18) and the effective PS decay constant (Fig. 19). We will comment on the effective PS mass, but all the observations will be equally valid for the effective PS decay constant.

The first observation is that the effective masses from local sources are always decreasing with the Euclidean time. Therefore, if the temporal size is not large enough to contain the plateau of the effective mass, the estimated mass will be larger than the real one. On the other hand the effective masses from wall-smearred sources for on this ensemble are increasing (although this is not true across all ensembles). Therefore, if the plateau is not reached, the estimated mass will be smaller than the real one.

Consider now the 24×12^3 effective masses in Fig. 18. The local and wall-smearred sources give effective masses whose quality in terms of flatness is similar (compare with Fig. 6b), and the plateau is not clearly visible in any of the effective masses. However since the gap between the local and wall-smearred effective masses closes down in the midpoint $t = 12$, one can argue that the plateau is effectively reached there.

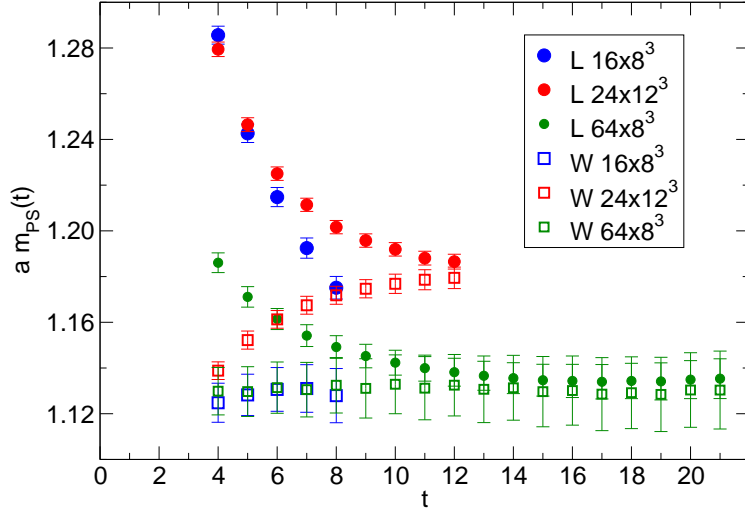


Figure 18: Effective PS mass on different volumes for $am_0 = -1.05$ and $\beta = 2.25$ (L=local, W=wall). At t larger than 21, this quantity (on the 64×8^3) becomes much noisier and we cut it for sake of clarity.

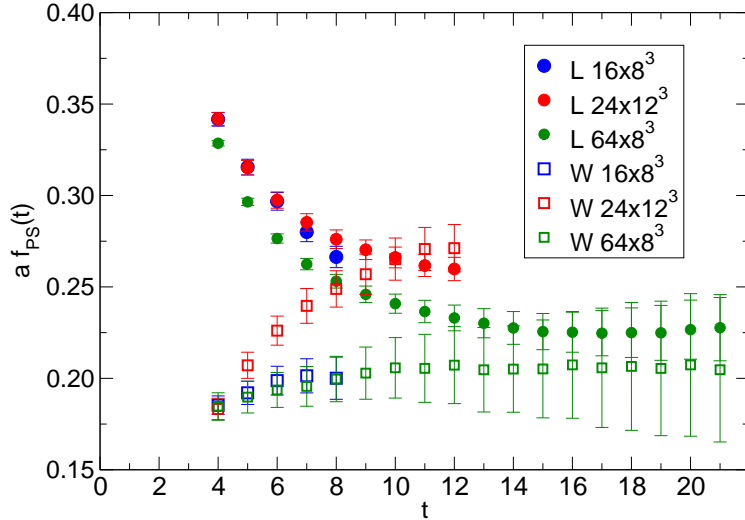


Figure 19: Effective PS decay constant on different volumes for $am_0 = -1.05$ and $\beta = 2.25$ (L=local, W=wall). At t larger than 21, this quantity (on the 64×8^3) becomes much noisier and we cut it for the sake of clarity.

The situation is completely different for the 16×8^3 . The gap between the local and wall-smearred effective masses is always quite big. The wall-smearred source gives a much flatter effective mass than the local source (compare with Fig. 6a). In order to obtain a more precise estimate for the pseudoscalar mass on the spatial volume 8^3 , we simulated on a 64×8^3 lattice. In this case the temporal extent is large enough to obtain very good plateaux for both the local and wall-smearred effective masses.

By comparing the effective masses on the 24×12^3 and 64×8^3 lattices it is clear that the finite volume has the effect of making the pseudoscalar meson lighter. What is happening then with the 16×8^3 lattice? The mass estimated with the local sources is affected by two relatively large effects: the finite volume, which decreases the mass and the bad determination of the plateaux, which increases the mass. Having opposite sign and accidentally the same magnitude, these two effects cancel each other. Therefore the finite volume effects are actually larger than what we estimated on the basis of the local sources, and they are better estimated using the wall-smearred source at light enough masses.

The conclusions above are valid also for the vector meson mass and for the ratio M_V/M_{PS} . In particular from Fig. 11 it is clear that on increasing the spatial volume, the ratio M_V/M_{PS} slightly increases, and this effect was completely hidden in the local-source determination.

6 Conclusions

In this article we have studied systematic effects on the PCAC mass, the mesonic masses and decay constants due to a short temporal size on the SU(2) gauge theory with two Dirac fermions in the adjoint representation. In order to isolate the ground state in correlators one should take the source and sink infinitely distant. In practice one defines effective quantities (masses and decay constants) which depend on the time separation between source and sink, and which show a plateau at large distances. The value of the plateau gives an estimate for the corresponding mass or decay constant. At fixed temporal extent one can increase the relative amplitude of the ground state in correlators, using smeared sources and/or sinks. This translates into flatter and longer plateaux in the effective quantities.

We have extended the *Chroma* suite of software in order to operate with fermions in the adjoint representation of the gauge group, and we have used the *Chroma* built-in routines for measuring mesonic correlators with both Gaussian and wall-smearred sources. We observe that at our lightest masses the wall-smearing gives always the best overlap with the ground state. At heavy masses the mesonic wave functions are more localized and the local sources give a better overlap with the ground state. There is an intermediate regime of masses in which the local and wall-smearing sources yield plateaux of similar quality. In this case a Gaussian smearing with properly chosen width might be desirable. If one wants a procedure that enhance the overlap with the ground state at any mass, one should use a variational method with a large set of smeared sources. However, since the interesting physical region is close to the chiral limit, we chose simplicity against generality and we focused our detailed analysis on the wall-smearing only.

The enhancement of the plateaux with smeared sources does not come for free. Ob-

servables obtained with smeared sources have longer autocorrelation times. For a fixed set of configurations, a better control on the systematic error with respect to local sources is generally obtained at the cost of a larger statistical uncertainty.

Among the observables that we have considered, the PCAC mass is the least affected by the systematics, while the decay constants are the most affected. In the region $aM_{PS} < 0.5$, the 16×8^3 lattice yields relative systematic errors for the PS mass larger than 10%. At least the 24×12^3 lattice is needed in order to stay below 10%.

We also investigated how the finite temporal extent can conspire to partially mask effects due to finite spatial volume, and discovered that finite-volume effects were underestimated in our analysis with local sources. The relative difference between the determinations of the PS mass on the 16×8^3 and 24×12^3 lattices is of order 5% at $aM_{PS} \simeq 1$ and it goes up to 14% at about $aM_{PS} \simeq 0.3$. Again, in the interesting region of masses, the 16×8^3 lattice appears to be way too far from the infinite volume limit. A detailed study of finite-volume effects is extremely important in order to address issues like IR-conformality, and represents one of our major research lines.

Finally we notice that our conclusions regarding the near-conformal dynamics of this theory are robust, since the main qualitative features already presented in Refs. [22, 25] are confirmed by the present analysis.

Acknowledgements

The numerical calculations presented in this work have been performed on the Horseshoe6 cluster at the University of Southern Denmark (SDU) funded by the Danish Centre for Scientific Computing for the project “Origin of Mass” 2009/2010. EK is supported by SUPA, the Scottish Universities Physics Alliance. AR thanks the Deutsche Forschungsgemeinschaft for financial support. BL is supported by the Royal Society. AP was supported by the EC (Research Infrastructure Action in FP7, project *HadronPhysics2*). The development of the code used in this work was partially supported by the EPSRC grant EP/F010303/1. We thank the DEISA Consortium (www.deisa.eu), funded through the EU FP7 project RI-222919, for support within the DEISA Extreme Computing Initiative. LDD and BL would like to thank the GGI in Florence for hospitality during the final stage of this work.

Appendices

A Correlators and smearings

A.1 Local correlators

In order to measure mesonic observables we measure zero-momentum correlators of the form

$$f_{\Gamma\Gamma'}(t) = \sum_{\vec{x}} \langle \mathcal{O}_{\Gamma}^{SINK\dagger}(\vec{x}, t) \mathcal{O}_{\Gamma'}^{SRCE}(\vec{0}, 0) \rangle, \quad (\text{A.1})$$

where $\mathcal{O}_{\Gamma}^{SRCE, SINK}$ are interpolating quark bilinear operators with the correct symmetries under spin and parity. We require the isospin non-singlet correlators and so, for example, we could construct a *local* correlator with the most immediate choice

$$\mathcal{O}_{\Gamma}^{SRCE}(\vec{x}, t) = \mathcal{O}_{\Gamma}^{SINK}(\vec{x}, t) = \bar{\psi}_1(\vec{x}, t) \Gamma \psi_2(\vec{x}, t), \quad (\text{A.2})$$

where the labels i on the quark fields ψ_i denotes the fermion flavour. Here Γ is a matrix in the Dirac algebra, which determines the symmetries of the operator. This choice reproduces the correlators considered in [25]:

$$f_{\Gamma\Gamma'}^L(t) = \sum_{\vec{x}} \langle (\bar{\psi}_1(\vec{x}, t) \Gamma \psi_2(\vec{x}, t))^\dagger \bar{\psi}_1(\vec{0}, 0) \Gamma' \psi_2(\vec{0}, 0) \rangle, \quad (\text{A.3})$$

where here the superscript on $f_{\Gamma\Gamma'}$ indicates the local choice. This correlator is measured by computing the quark propagator $S(\vec{x}, t; \vec{x}', t')$, in terms of which

$$f_{\Gamma\Gamma'}^L(t) = -\frac{a^3}{V_s} \sum_{\vec{x}} \text{Tr}[\gamma_0 \Gamma^\dagger \gamma_0 S(\vec{x}, t; \vec{0}, 0) \Gamma' \gamma_5 S(\vec{x}, t; \vec{0}, 0)^\dagger \gamma_5]. \quad (\text{A.4})$$

The propagator is computed by solving the equation

$$a^4 \sum_{\mathbf{y}} D(\mathbf{x}; \mathbf{y}) S(\mathbf{y}, \mathbf{z}) = I \delta_{\mathbf{x}; \mathbf{z}}, \quad (\text{A.5})$$

where the boldface variables denote the full space-time coordinate, I denotes the identity matrix in spin and colour space, and $D(\mathbf{x}; \mathbf{y})$ is the Dirac matrix.

A.2 Extended quark fields

In order to obtain an optimum signal for the masses we aim to extract from these correlators, we should construct interpolating operators with a maximised overlap with the desired ground state. The local operators (A.2) are not expected to satisfy this requirement well, as the mesons typically have an extension of many times the lattice spacing

in a typical simulation. We can improve the situation by considering an operator which is extended spatially over the lattice:

$$\mathcal{O}_\Gamma(\vec{x}, t) = \sum_{\vec{y}_1, \vec{y}_2} \Psi(\vec{x}, \vec{y}_1, \vec{y}_2) \bar{\psi}_1(\vec{y}_1, t) \Gamma \psi_2(\vec{y}_2, t). \quad (\text{A.6})$$

Usually shell-model wave functions are used [33], meaning the positions of the quark and antiquark are decoupled:

$$\Psi(\vec{x}, \vec{y}_1, \vec{y}_2) = \phi(\vec{x}, \vec{y}_1) \phi(\vec{x}, \vec{y}_2). \quad (\text{A.7})$$

The choice $\phi(\vec{x}, \vec{y}) = \delta_{\vec{x}, \vec{y}}$ reproduces the point-point case (A.2).

In general, such wave functions are not gauge invariant, and as such any expectation value over an ensemble of gauge configurations, in which they are used, must vanish, according to Elitzur's theorem [34]. To avoid this we can fix the gauge on each configuration, being careful to check for errors introduced by the issue of Gribov copies.

Using $\phi^{SRCE/SINK}$ to define $\mathcal{O}^{SRCE/SINK}$ we see that our correlation function can be computed as

$$f_{\Gamma\Gamma'}(t) = - \sum_{\vec{x}} \text{Tr}[\gamma_0 \Gamma^\dagger \gamma_0 \hat{S}(\vec{x}, t; \vec{0}, 0) \Gamma' \gamma_5 \hat{S}(\vec{x}, t; \vec{0}, 0)^\dagger \gamma_5], \quad (\text{A.8})$$

where $\hat{S}(\vec{x}, t; \vec{x}', t')$ is defined as

$$\hat{S}(\vec{x}, t; \vec{x}', t') = \sum_{\vec{y}, \vec{y}'} S(\vec{y}, t; \vec{y}', t') \phi^{SINK}(\vec{x}, \vec{y}) \phi^{SRCE}(\vec{x}', \vec{y}'). \quad (\text{A.9})$$

It can be easily seen that if we solve for S' , the system

$$a^4 \sum_{\mathbf{y}} D(\mathbf{x}, \mathbf{y}) S'(\mathbf{y}, \mathbf{z}) = \phi^{SRCE}(\vec{z}, \vec{x}) \delta_{x_0, z_0}, \quad (\text{A.10})$$

we can compute \hat{S} as

$$\hat{S}(\vec{x}, t; \vec{x}', t') = \sum_{\vec{y}} S'(\vec{y}, t; \vec{x}', t') \phi^{SINK}(\vec{x}, \vec{y}). \quad (\text{A.11})$$

In fact it is the choice of a shell-model type wave-function (A.7) that allows us to calculate the correlation function using only one inversion of the Dirac matrix (per colour and spin index).

A.3 Smearing examples

A simple guess for an effective form of $\phi(\vec{x})$ is in the form of a gaussian

$$\phi(\vec{x}, \vec{y}) = e^{-\left(\frac{|\vec{x}-\vec{y}|}{R}\right)^2}, \quad (\text{A.12})$$

where $R > 0$ is some effective radius chosen to represent the wave function of the meson of interest. The choice $\frac{1}{R} \rightarrow 0$ results in $\phi(\vec{x}, \vec{y})$ having equal weight over the whole lattice, and is termed a *wall smearing*.

On a lattice we can approximate the gaussian as the limit of the iterative form

$$\phi(\vec{x}, \vec{y}) = \left(1 - \frac{w^2}{4N} \square\right)^N \delta_{\vec{x}, \vec{y}}, \quad (\text{A.13})$$

where \square is the lattice version of the Laplacian

$$\square(\vec{x}, \vec{y}) = \sum_{i=1}^3 (\delta_{\vec{x}, \vec{y}-\hat{i}} + \delta_{\vec{x}, \vec{y}+\hat{i}}). \quad (\text{A.14})$$

(A.13) then approximates (A.12) in the limit $N \rightarrow \infty$, with the radius R being determined by w . Replacing \square with its covariant form

$$\square(\vec{x}, \vec{y}; t) = \sum_{i=1}^3 \left(U_i(\vec{x}, t) \delta_{\vec{x}, \vec{y}-\hat{i}} + U_i^\dagger(\vec{x} - \hat{i}, t) \delta_{\vec{x}, \vec{y}+\hat{i}} \right), \quad (\text{A.15})$$

results in a gauge invariant operator, negating the requirement for gauge fixing. This choice of ϕ is called *gauge-invariant gaussian smearing*.

We have utilised both a wall-smearing (denoted W) and a gauge-invariant gaussian smearing (denoted G) in our study.

A.4 Gauge fixing

When constructing a correlator involving the gauge-dependent wall-smearred quark bilinear, we must fix the gauge on each configuration with which we wish to work. We fix to Coulomb gauge by generating a gauge-fixed gauge configuration from the original by maximising the quantity $\sum_{\mathbf{x}} \sum_{i=1}^3 \text{Re}(\text{Tr}[U_i(\mathbf{x})])$.

B Meson correlator phenomenology

B.1 Meson masses

We extract the meson masses from our theory by analysing correlators of the form (A.1) in the case where we consider source and sink operators with equal symmetries, i.e. $\Gamma = \Gamma'$, and so we shall write $f_{\Gamma\Gamma} = f_\Gamma$. We can write f_Γ explicitly as an expectation value on the vacuum state $|0\rangle$:

$$f_\Gamma(t) = \sum_{\vec{x}} \langle 0 | \mathcal{O}_\Gamma^{SINK^\dagger}(\vec{x}, t) \mathcal{O}_\Gamma^{SRCE}(\vec{0}, 0) | 0 \rangle. \quad (\text{B.1})$$

Labelling the energy eigenstates of the theory as $|n, \vec{p}\rangle$, we can write a complete set of states as

$$\sum_n \int \frac{d^3p}{(2\pi)^3 2E_n(\vec{p})} |n, \vec{p}\rangle \langle n, \vec{p}|. \quad (\text{B.2})$$

We can insert this in f_Γ producing

$$f_\Gamma(t) = \sum_n \sum_{\vec{x}} \int \frac{d^3p}{(2\pi)^3 2E_n(\vec{p})} \langle 0 | \mathcal{O}_\Gamma^{SINK^\dagger}(\vec{x}, t) | n, \vec{p}\rangle \langle n, \vec{p}| \mathcal{O}_\Gamma^{SRCE}(\vec{0}, 0) | 0 \rangle. \quad (\text{B.3})$$

Translating $\mathcal{O}^{SINK}(\mathbf{x})$ to the origin produces $e^{i\mathcal{P}\cdot\mathbf{x}}\mathcal{O}^{SINK}(\mathbf{0})e^{-i\mathcal{P}\cdot\mathbf{x}}$ where the four-momentum operator $\mathcal{P} = \{\mathcal{H}, \vec{\mathcal{P}}\}$ giving

$$\langle 0|\mathcal{O}_\Gamma^{SINK^\dagger}(\vec{x}, t)|n, \vec{p}\rangle = \langle 0|\mathcal{O}_\Gamma^{SINK^\dagger}(\mathbf{0})|n, \vec{p}\rangle e^{-i\mathbf{P}\cdot\mathbf{x}}, \quad (\text{B.4})$$

where $\mathbf{p} = \{E_n(\vec{p}), \vec{p}\}$. As a result, the sum over the spatial position \vec{x} collapses the sum onto zero-momentum

$$f_\Gamma(t) = \sum_n \frac{1}{2E_n} \langle 0|\mathcal{O}_\Gamma^{SINK^\dagger}(\vec{0}, 0)|n\rangle \langle n|\mathcal{O}_\Gamma^{SRCE}(\vec{0}, 0)|0\rangle e^{-iE_n t}, \quad (\text{B.5})$$

where we denote $|n, \vec{0}\rangle$ as $|n\rangle$ and $E_n(\vec{0})$ as E_n . The overlaps $\langle 0|\mathcal{O}(\mathbf{0})|n\rangle$ will vanish for all states except those with the same symmetries as \mathcal{O}_Γ and we can see that at large Euclidean time $\tau = it$ the correlator is dominated by the lowest in energy of such states which we denote $|\Gamma\rangle$ with energy E_Γ which as we are at zero momentum equals the mass of the state $E_\Gamma = m_\Gamma$:

$$\begin{aligned} f_\Gamma(\tau) &\xrightarrow{\tau \rightarrow \infty} \frac{1}{2m_\Gamma} \langle 0|\mathcal{O}_\Gamma^{SINK^\dagger}(\vec{0}, 0)|\Gamma\rangle \langle \Gamma|\mathcal{O}_\Gamma^{SRCE}(\vec{0}, 0)|0\rangle e^{-m_\Gamma \tau} \\ &\equiv A_\Gamma e^{-m_\Gamma \tau}. \end{aligned} \quad (\text{B.6})$$

On a lattice with finite temporal extent $0 < \tau < L_t$, this asymptotic behaviour is modified by the appearance of an extra term corresponding to a quark propagating backward from source to sink through the anti-periodic boundary:

$$\begin{aligned} f_\Gamma(\tau) &\rightarrow A_\Gamma (e^{-m_\Gamma \tau} + e^{-m_\Gamma(L_t - \tau)}) \\ &\equiv A_\Gamma hc(\tau, m_\Gamma, L_t). \end{aligned} \quad (\text{B.7})$$

In this way we can extract the meson masses from the exponential behaviour of the f_Γ at large Euclidean time.

As in [25], we use the Prony method [35] to solve this system, to produce an ‘‘effective mass’’ $m_\Gamma(\tau)$ which as a function of the lattice temporal coordinate is expected to approach the desired mass in the limit of large times $m_\Gamma(t) \xrightarrow{\tau \rightarrow \infty} m_\Gamma$. The meson mass is extracted by choosing a region around the centre of the temporal axis and fitting the effective mass to a constant in this region.

In our study we have considered the case $\Gamma = \gamma_5$, defining the *pseudoscalar* channel, with mass m_{PS} and the degerate cases $\Gamma = \gamma_i$ $i \in \{1, 2, 3\}$, defining the *vector* channel with mass m_{V} . In practice the correlators f_{γ_i} are averaged to produce a single correlator for the vector channel. We call the resulting vector correlator f_{VV} and the pseudoscalar correlator f_{PP} .

The masses can be extracted identically from these correlators regardless of the smearing used. In practice it is found that correlators with a smeared source are preferred to local correlators for this purpose, in that they produce an improved signal to noise ratio for the masses. Correlators with smearing at both the source and sink are found to be disfavoured because of enhanced fluctuations.

B.2 Amplitudes

If local quark fields are used, $\mathcal{O}_\Gamma^{SRCE/SINK}(\mathbf{x}) = \bar{\psi}_1(\mathbf{x})\Gamma\psi_2(\mathbf{x}) = \mathcal{O}_\Gamma^L(\mathbf{x})$. In the case of both the pseudoscalar and vector channels, we are interested in the quantity $|\langle 0|\mathcal{O}_\Gamma^L(\mathbf{0})|\Gamma\rangle|$ although they have different meanings:

$$|\langle 0|\mathcal{O}_{\gamma_5}^L(\mathbf{0})|\gamma_5\rangle| \equiv G_{\text{PS}}, \quad (\text{B.8})$$

$$|\langle 0|\mathcal{O}_{\gamma_i}^L(\mathbf{0})|\gamma_i\rangle| \equiv \epsilon_i F_V m_V,$$

where ϵ_i is a polarisation tensor. We call G_{PS} the *pseudoscalar vacuum to meson amplitude* (or, more commonly, simply the pseudoscalar amplitude), and F_V is the *vector decay constant*. We can easily construct effective observables for these quantities from the local correlators f_{PP}^L and f_{VV}^L :

$$G_{\text{PS}}^L(\tau) = \sqrt{\frac{2m_{\text{PS}}(\tau)f_{\text{PP}}^L(\tau)}{hc(\tau, m_{\text{PS}}(\tau), L_t)}}, \quad (\text{B.9})$$

$$F_V^L(\tau) = \sqrt{\frac{2f_{\text{VV}}^L(\tau)}{m_V hc(\tau, m_V(\tau), L_t)}}.$$

If we wish to use smeared operators to extract these quantities, the amplitudes in (B.6) are, in general, no longer related to the quantities of interest (B.8). However, if our correlator involves only a smearing at the source, with a local sink, we see that the sink amplitude in (B.6) is still of the correct form (B.8). We need cancel the other undesired amplitude, introduced by the smearing. We can do this by combining our local-smeared correlator (f_Γ^{LS}) with a smeared-smeared correlator (f_Γ^{SS}). Effective observables equivalent to (B.8) can be defined from smeared correlators as

$$G_{\text{PS}}^S(\tau) = \sqrt{\frac{2m_{\text{PS}}(\tau)}{hc(\tau, m_{\text{PS}}(\tau), L_t)} \frac{f_{\text{PP}}^{LS^2}(\tau)}{f_{\text{PP}}^{SS}(\tau)}}, \quad (\text{B.10})$$

$$F_V^S(\tau) = \sqrt{\frac{2}{m_V hc(\tau, m_V(\tau), L_t)} \frac{f_{\text{VV}}^{LS^2}(\tau)}{f_{\text{VV}}^{SS}(\tau)}}.$$

B.3 Quark Mass

As our simulation is based on the Wilson quark formulation, the physical quark mass in our simulation m is related to the bare quark mass which is an input to the simulation m_0 by an additive renormalisation, which being a non-perturbative quantity can not be calculated a priori. As such we must have a method of determining the physical quark mass in the simulation in order to determine our proximity to the chiral point $m = 0$ and to observe the scaling of mesonic observables with m .

The most straight-forward such method is via the *partially conserved axial current mass* or PCAC mass. We define the continuum non-singlet axial and pseudoscalar currents as

$$A_\mu(\mathbf{x}) = \bar{\psi}_1(\mathbf{x})\gamma_\mu\gamma_5\psi_2(\mathbf{x}), \quad P(\mathbf{x}) = \bar{\psi}_1(\mathbf{x})\gamma_5\psi_2(\mathbf{x}). \quad (\text{B.11})$$

We see that these are continuum versions of our $\mathcal{O}_{\gamma_\mu\gamma_5}^L$ and $\mathcal{O}_{\gamma_5}^L$. From the Ward identity for the axial transformation $\psi \rightarrow e^{i\alpha\gamma_5}\psi$ we obtain for the divergence of the axial current

$$\partial_\mu A_\mu(\mathbf{x}) = -2mP(\mathbf{x}), \quad (\text{B.12})$$

where m is the physical quark mass, as above. From this we obtain

$$\frac{\partial}{\partial t} \int d^3x \langle A_0(\vec{x}, t) \mathcal{O}_{\gamma_5} \rangle = -2m \langle P(\vec{x}, t) \mathcal{O}_{\gamma_5} \rangle, \quad (\text{B.13})$$

where \mathcal{O}_{γ_5} is any bilinear quark operator with the symmetries of a pseudoscalar current. Taking a lattice version of this, and choosing for \mathcal{O}_{γ_5} any of the local or smeared lattice pseudoscalar currents we have previously constructed, we see we can define an effective PCAC quark mass via

$$m(\tau) = \frac{m_{\text{PS}}}{\sinh(am_{\text{PS}})} \frac{f_{\text{AP}}^{LS}(\tau - a) - f_{\text{AP}}^{LS}(\tau + a)}{4f_{\text{PP}}^{LS}(\tau)}, \quad (\text{B.14})$$

where we define f_{AP} to be $f_{\gamma_0\gamma_5, \gamma_5}$. The prefactor of $\frac{m_{\text{PS}}}{\sinh(am_{\text{PS}})}$ arises by a choice of the lattice finite difference operator which more accurately represents the continuum derivative on f_{AP} . The correlators f^{LS} are constructed with a local sink, and a source which can be local, or involve any smearing.

B.4 Pseudoscalar decay constant

Similarly to (B.6) the correlator f_{AP} has an asymptotic behaviour:

$$\begin{aligned} f_{\text{AP}}(\tau) &\xrightarrow{\tau \rightarrow \infty} \frac{1}{2m_{\text{PS}}} \langle 0 | \mathcal{O}_{\gamma_0\gamma_5}^{\text{SINK}\dagger}(\vec{0}, 0) | \gamma_5 \rangle \langle \gamma_5 | \mathcal{O}_{\gamma_5}^{\text{SRCE}}(\vec{0}, 0) | 0 \rangle e^{-m_{\text{PS}}\tau} \\ &\equiv A_{\text{AP}} e^{-m_{\text{PS}}\tau}. \end{aligned} \quad (\text{B.15})$$

In contrast to (B.7) however, the contribution to f_{AP} from propagation around the lattice comes with the opposite sign, so on a lattice with finite temporal extent,

$$\begin{aligned} f_{\text{AP}}(\tau) &\rightarrow A_{\text{AP}} (e^{-m_{\text{PS}}\tau} - e^{-m_{\text{PS}}(L_t - \tau)}) \\ &\equiv A_{\text{AP}} h_S(\tau, m_{\text{PS}}, L_t). \end{aligned} \quad (\text{B.16})$$

Now we define the *pseudoscalar decay constant* F_{PS} as

$$m_{\text{PS}} F_{\text{PS}} = \langle 0 | \mathcal{O}_{\gamma_0\gamma_5}^L(\vec{0}, 0) | \gamma_5 \rangle. \quad (\text{B.17})$$

Combining this with the Ward identity for f_{AP} we can define an effective observable for F_{PS} as

$$F_{\text{PS}}^S(\tau) = \frac{2m(\tau)G_{\text{PS}}^S(\tau)}{m_{\text{PS}}^2(\tau)}. \quad (\text{B.18})$$

The superscript S here indicates that this is valid for observables obtained from any smeared correlator, provided the corresponding definition of G_{PS} is used, from (B.9) or (B.10).

C Results tables

lattice	$-am_0$	N_{conf}	am	am_{PS}	am_V	aF_{PS}	aF_V
S0	-0.5	901	1.16353(73)	2.7983(15)	2.8042(16)	0.2950(73)	0.3338(92)
S1	-0.25	901	1.07205(97)	2.6535(21)	2.6613(22)	0.3150(63)	0.3629(80)
S2	0	901	0.9706(11)	2.4938(25)	2.5045(27)	0.3335(63)	0.3935(84)
S3	0.25	901	0.8552(11)	2.3092(28)	2.3241(31)	0.3579(74)	0.435(10)
S4	0.5	901	0.7224(13)	2.0934(32)	2.1155(37)	0.3729(87)	0.475(13)
S5	0.75	901	0.5607(18)	1.8136(47)	1.8473(55)	0.375(12)	0.511(21)
S6	0.9	901	0.4330(18)	1.5582(68)	1.5987(81)	0.315(13)	0.441(23)
A0	0.95	1501	0.3849(16)	1.4488(68)	1.4902(84)	0.291(12)	0.411(22)
A1	0.975	1499	0.3582(17)	1.3830(74)	1.4251(91)	0.274(11)	0.388(21)
A2	1	7300	0.3314(19)	1.3137(78)	1.3553(97)	0.258(13)	0.368(23)
A3	1.025	1481	0.3001(19)	1.2222(90)	1.260(11)	0.230(10)	0.324(18)
A4	1.05	1481	0.2688(15)	1.1290(83)	1.1645(99)	0.1970(64)	0.2692(89)
A5	1.075	1277	0.2352(18)	1.011(13)	1.042(16)	0.185(11)	0.258(20)
A6	1.1	1279	0.1992(32)	0.886(14)	0.914(19)	0.1642(99)	0.227(17)
A7	1.125	1344	0.1595(25)	0.725(14)	0.747(18)	0.1478(76)	0.200(15)
A8	1.15	1278	0.1150(31)	0.519(18)	0.534(23)	0.1439(70)	0.194(10)
A9	1.175	1280	0.0628(30)	0.285(23)	0.295(30)	0.1569(43)	0.2120(81)

Table 1: Results for mesonic observables from wall-smearred correlators on a 16×8^3 lattice at $\beta = 2.25$.

lattice	$-am_0$	N_{conf}	am	am_{PS}	am_V	aF_{PS}	aF_V
B0	0.95	1973	0.39017(68)	1.4720(23)	1.5186(28)	0.3220(61)	0.468(11)
B1	1	1689	0.33623(82)	1.3441(28)	1.3932(37)	0.2942(73)	0.434(13)
B2	1.05	1564	0.27470(91)	1.1782(39)	1.2252(51)	0.269(11)	0.395(19)
B3	1.075	1438	0.2393(10)	1.0660(55)	1.1058(68)	0.231(13)	0.333(24)
B4	1.1	5112	0.2014(10)	0.9310(65)	0.9638(79)	0.1523(85)	0.208(14)
B5	1.125	1240	0.16013(92)	0.7697(60)	0.7963(68)	0.1485(63)	0.2062(97)
B6	1.15	640	0.1149(15)	0.572(12)	0.588(15)	0.0955(53)	0.1296(89)
B7	1.175	5137	0.0653(14)	0.3277(95)	0.336(11)	0.0985(33)	0.1298(54)
B8	1.18	818	0.0547(17)	0.282(11)	0.294(13)	0.0984(53)	0.1311(78)
B9	1.185	840	0.0418(16)	0.206(11)	0.213(11)	0.1056(43)	0.1366(63)
B10	1.19	700	0.0300(11)	0.1476(82)	0.1539(96)	0.1129(32)	0.1496(36)

Table 2: Results for mesonic observables from wall-smearred correlators on a 24×12^3 lattice at $\beta = 2.25$.

lattice	$-am_0$	N_{conf}	am	am_{PS}	am_V	aF_{PS}	aF_V
C0	1.15	1090	0.11731(77)	0.6121(64)	0.6305(83)	0.0983(44)	0.1314(87)
C1	1.175	523	0.06579(77)	0.3652(87)	0.381(10)	0.0746(35)	0.1037(64)
C2	1.18	917	0.05437(79)	0.3042(69)	0.3174(80)	0.0736(37)	0.0992(59)
C3	1.185	864	0.04217(84)	0.2241(62)	0.2297(72)	0.0763(32)	0.0992(44)
C4	1.19	1083	0.03065(72)	0.1682(62)	0.1764(64)	0.0776(27)	0.1038(36)

Table 3: Results for mesonic observables from wall-smearred correlators on a 32×16^3 lattice at $\beta = 2.25$.

lattice	$-am_0$	N_{conf}	am	am_{PS}	am_V	aF_{PS}	aF_V
D0	1.18	185	0.05528(25)	0.3239(49)	0.3295(62)	0.0398(27)	0.0455(41)
D1	1.185	164	0.04287(29)	0.2462(58)	0.2566(75)	0.0696(65)	0.091(11)
D2	1.19	160	0.02967(50)	0.1741(52)	0.1759(59)	0.0501(30)	0.0601(52)

Table 4: Results for mesonic observables from wall-smearred correlators on a 64×24^3 lattice at $\beta = 2.25$.

lattice	$-am_0$	N_{conf}	am	am_{PS}	am_V	aF_{PS}	aF_V
E0	1.25	131	0.11751(28)	0.7173(11)	0.7735(39)	0.1592(26)	0.263(12)
E1	1.26	130	0.08527(34)	0.5612(15)	0.5881(45)	0.1122(26)	0.169(11)

Table 5: Results for mesonic observables from wall-smearred correlators on a 64×24^3 lattice at $\beta = 2.1$.

lattice	$-am_0$	am_{PS}^2/m	m_V/F_{PS}	m_V/m_{PS}	$a^3(m_{PS}F_{PS})^2/m$	F_V/F_{PS}
S0	-0.5	6.7300(39)	9.50(23)	1.002100(47)	0.586(29)	1.1311(35)
S1	-0.25	6.5681(57)	8.45(16)	1.00294(10)	0.652(26)	1.1520(29)
S2	0	6.4070(67)	7.51(13)	1.00428(14)	0.713(27)	1.1797(37)
S3	0.25	6.2347(86)	6.49(13)	1.00647(22)	0.798(33)	1.2172(50)
S4	0.5	6.065(10)	5.67(12)	1.01058(36)	0.844(40)	1.2754(72)
S5	0.75	5.866(17)	4.91(16)	1.01858(75)	0.830(57)	1.359(14)
S6	0.9	5.606(31)	5.07(19)	1.0259(11)	0.558(49)	1.398(18)
A0	0.95	5.453(33)	5.11(19)	1.0286(13)	0.465(41)	1.408(19)
A1	0.975	5.338(37)	5.20(20)	1.0303(15)	0.402(37)	1.414(18)
A2	1	5.206(40)	5.24(24)	1.0316(17)	0.350(36)	1.421(24)
A3	1.025	4.977(47)	5.47(22)	1.0308(19)	0.265(26)	1.405(21)
A4	1.05	4.741(48)	5.91(16)	1.0314(18)	0.184(13)	1.366(18)
A5	1.075	4.352(94)	5.63(29)	1.0300(50)	0.150(21)	1.390(32)
A6	1.1	3.94(10)	5.58(27)	1.0310(70)	0.107(14)	1.385(37)
A7	1.125	3.299(93)	5.06(20)	1.0307(70)	0.0724(87)	1.358(54)
A8	1.15	2.35(13)	3.71(17)	1.028(16)	0.0489(60)	1.350(31)
A9	1.175	1.30(19)	1.88(20)	1.034(44)	0.0320(48)	1.351(39)

Table 6: Ratios of mesonic observables from wall-smearred correlators on a 16×8^3 lattice at $\beta = 2.25$.

lattice	$-am_0$	am_{PS}^2/m	m_V/F_{PS}	m_V/m_{PS}	$a^3(m_{PS}F_{PS})^2/m$	F_V/F_{PS}
B0	0.95	5.553(10)	4.717(84)	1.03166(59)	0.576(22)	1.454(12)
B1	1	5.373(13)	4.73(11)	1.03652(96)	0.465(23)	1.476(20)
B2	1.05	5.053(21)	4.55(17)	1.0398(13)	0.367(31)	1.465(19)
B3	1.075	4.748(35)	4.79(26)	1.0373(21)	0.255(30)	1.438(31)
B4	1.1	4.303(42)	6.34(32)	1.0352(18)	0.100(11)	1.365(27)
B5	1.125	3.700(42)	5.36(20)	1.0345(18)	0.0818(77)	1.388(14)
B6	1.15	2.84(10)	6.17(26)	1.0287(85)	0.0261(35)	1.355(38)
B7	1.175	1.644(71)	3.41(12)	1.026(12)	0.0160(14)	1.317(25)
B8	1.18	1.457(93)	2.99(19)	1.042(21)	0.0141(18)	1.332(30)
B9	1.185	1.022(90)	2.02(12)	1.034(23)	0.0114(12)	1.293(44)
B10	1.19	0.727(68)	1.36(10)	1.043(32)	0.00926(75)	1.325(37)

Table 7: Ratios of mesonic observables from wall-smearred correlators on a 24×12^3 lattice at $\beta = 2.25$.

lattice	$-am_0$	am_{PS}^2/m	m_V/F_{PS}	m_V/m_{PS}	$a^3(m_{PS}F_{PS})^2/m$	F_V/F_{PS}
C0	1.15	3.194(53)	6.41(25)	1.0299(47)	0.0310(30)	1.334(40)
C1	1.175	2.028(87)	5.12(21)	1.045(10)	0.0113(14)	1.389(37)
C2	1.18	1.702(62)	4.32(20)	1.043(10)	0.0092(10)	1.348(28)
C3	1.185	1.191(55)	3.01(13)	1.024(16)	0.00696(68)	1.298(23)
C4	1.19	0.924(57)	2.27(11)	1.048(20)	0.00557(46)	1.336(26)

Table 8: Ratios of mesonic observables from wall-smearred correlators on a 32×16^3 lattice at $\beta = 2.25$.

lattice	$-am_0$	am_{PS}^2/m	m_V/F_{PS}	m_V/m_{PS}	$a^3(m_{PS}F_{PS})^2/m$	F_V/F_{PS}
D0	1.18	1.899(55)	8.29(45)	1.0169(88)	0.00304(51)	1.140(47)
D1	1.185	1.414(64)	3.70(28)	1.042(14)	0.0069(15)	1.308(59)
D2	1.19	1.023(53)	3.51(17)	1.009(19)	0.00259(42)	1.199(54)

Table 9: Ratios of mesonic observables from wall-smearred correlators on a 64×24^3 lattice at $\beta = 2.25$.

lattice	$-am_0$	am_{PS}^2/m	m_V/F_{PS}	m_V/m_{PS}	$a^3(m_{PS}F_{PS})^2/m$	F_V/F_{PS}
E0	1.25	4.378(10)	4.857(81)	1.0783(49)	0.1110(37)	1.653(76)
E1	1.26	3.693(21)	5.24(12)	1.0479(79)	0.0465(22)	1.50(10)

Table 10: Ratios of mesonic observables from wall-smearred correlators on a 64×24^3 lattice at $\beta = 2.1$.

D Pull tables

lattice	V	$-am_0$	am	am_{PS}	a^2G_{PS}	aF_{PS}	am_V	aF_V
S0	16×8^3	-0.5	0.357743	0.630827	0.235108	0.256243	0.620554	0.183502
S1	16×8^3	-0.25	0.0890535	0.37089	0.25073	0.185906	0.364952	0.221968
S2	16×8^3	0	0.176656	0.103129	0.633081	0.570268	0.117478	0.603322
S3	16×8^3	0.25	0.0544221	0.89148	0.546006	0.402862	0.863709	0.524572
S4	16×8^3	0.5	0.41261	0.213066	0.74581	0.769548	0.198067	0.685742
S5	16×8^3	0.75	0.798726	0.721695	0.723448	0.773543	0.76452	0.658796
S6	16×8^3	0.9	0.914745	2.12396	2.85272	2.62616	2.19736	2.96989
A0	16×8^3	0.95	1.17047	2.87797	3.53652	3.17306	3.0289	3.70567
A1	16×8^3	0.975	1.48267	3.03748	3.0976	3.69649	3.1175	4.28469
A2	16×8^3	1	1.08558	3.30753	3.8366	3.39684	3.38991	3.99593
A3	16×8^3	1.025	1.50436	4.02795	5.56733	4.93876	4.08713	5.90623
A4	16×8^3	1.05	1.44732	4.8367	9.42537	8.00532	4.94294	12.0426
A5	16×8^3	1.075	0.854806	3.47175	6.88026	4.07907	3.40687	5.06541
A6	16×8^3	1.1	0.761814	3.25019	5.45758	4.42701	3.03732	5.34694
A7	16×8^3	1.125	1.07367	3.4146	5.77455	4.51791	3.05006	4.97578
A8	16×8^3	1.15	0.769772	2.64252	3.77974	2.61207	2.05669	3.82454
A9	16×8^3	1.175	0.567182	1.70204	1.91251	0.632631	1.61141	2.25052

Table 11: Pull of wall-smearred results from local results on 16×8^3 lattice.

lattice	V	$-am_0$	am	am_{PS}	a^2G_{PS}	aF_{PS}	am_V	aF_V
B0	24×12^3	0.95	0.774467	0.783603	1.42361	1.40895	0.871324	1.53757
B1	24×12^3	1	0.159875	1.40115	1.18323	0.807577	1.36064	1.46937
B2	24×12^3	1.05	0.457775	1.85951	0.417244	0.680213	2.01302	0.207503
B3	24×12^3	1.075	0.431929	2.35926	0.376053	0.0367313	2.57414	0.556833
B4	24×12^3	1.1	0.27378	4.08446	5.1113	4.65501	4.10009	5.44129
B5	24×12^3	1.125	0.0929123	4.42596	3.32675	1.76942	3.94236	2.57502
B6	24×12^3	1.15	0.886415	2.49618	4.85751	3.77226	2.04429	3.86822
B7	24×12^3	1.175	0.252409	2.90899	3.77684	1.8568	2.29301	2.32682
B8	24×12^3	1.18	0.623981	1.97381	2.98903	1.74813	1.6552	2.72508
B9	24×12^3	1.185	0.45537	1.69178	2.27698	0.544327	0.994413	2.10543
B10	24×12^3	1.19	0.107576	1.61624	1.86186	0.8264	0.831428	1.55631

Table 12: Pull of wall-smearred results from local results on 24×12^3 lattice.

lattice	V	$-am_0$	am	am_{PS}	a^2G_{PS}	aF_{PS}	am_V	aF_V
C0	32×16^3	1.15	0.0826998	2.76528	4.43289	3.49837	2.51094	3.69838
C1	32×16^3	1.175	0.656922	1.80444	3.88521	2.7899	1.63612	3.34912
C2	32×16^3	1.18	0.297786	2.34619	3.68642	2.42467	2.03804	3.61078
C3	32×16^3	1.185	0.0677226	2.36342	2.47807	0.443416	1.66751	1.68151
C4	32×16^3	1.19	0.13612	2.19063	3.10032	0.7232	1.75468	2.79363

Table 13: Pull of wall-smearred results from local results on 32×16^3 lattice.

lattice	V	$-am_0$	am	am_{PS}	a^2G_{PS}	aF_{PS}	am_V	aF_V
D0	64×24^3	1.18	0.231276	1.68437	10.7124	3.65489	1.98021	2.99979
D1	64×24^3	1.185	0.753454	0.491626	8.31795	2.83008	0.281183	1.97354
D2	64×24^3	1.19	0.302909	0.0376987	10.0776	0.153963	0.124777	0.183138

Table 14: Pull of wall-smearred results from local results on 64×24^3 lattice.

lattice	V	$-am_0$	am_{PS}^2/m	m_V/F_{PS}	m_V/m_{PS}	$a^3(m_{PS}F_{PS})^2/m$	F_V/F_{PS}
S0	16×8^3	-0.5	579.839	103.336	42.4374	14.8134	29.6658
S1	16×8^3	-0.25	355.964	115.643	28.3108	17.5745	40.2534
S2	16×8^3	0	256.472	102.845	27.2575	17.0714	36.0592
S3	16×8^3	0.25	161.5	76.8603	27.1434	13.7659	30.298
S4	16×8^3	0.5	105.789	55.6038	25.8027	10.1067	25.9244
S5	16×8^3	0.75	67.0073	41.9002	22.8086	6.02327	18.2194
S6	16×8^3	0.9	162.403	326	21.9192	10.0395	20.4498
A0	16×8^3	0.95	42.936	27.5523	19.6178	1.61548	14.8302
A1	16×8^3	0.975	34.6138	20.3632	18.5986	5.08223	15.0627
A2	16×8^3	1	29.2933	12.2385	15.9358	7.94612	10.4417
A3	16×8^3	1.025	27.2297	8.32147	13.3442	16.2042	10.4521
A4	16×8^3	1.05	27.2413	2.95847	13.634	32.67	7.68135
A5	16×8^3	1.075	16.7288	0.223305	3.82008	26.723	3.43554
A6	16×8^3	1.1	16.2186	2.76273	1.6808	24.4004	0.595224
A7	16×8^3	1.125	19.8065	2.29941	0.273288	21.8378	1.64239
A8	16×8^3	1.15	21.8515	4.29543	0.285916	27.8008	3.78825
A9	16×8^3	1.175	20.4856	11.9002	0.00540329	27.7572	3.35479

Table 15: Pull of wall-smearred results from local results on 16×8^3 lattice.

lattice	V	$-am_0$	am_{PS}^2/m	m_V/F_{PS}	m_V/m_{PS}	$a^3(m_{PS}F_{PS})^2/m$	F_V/F_{PS}
B0	24×12^3	0.95	0.396346	1.38681	0.71794	1.40066	0.62282
B1	24×12^3	1	0.495822	0.681721	0.7434	0.948186	1.25164
B2	24×12^3	1.05	0.562277	0.944498	1.53568	0.612448	2.12925
B3	24×12^3	1.075	1.16716	0.223536	1.73031	0.172471	1.35859
B4	24×12^3	1.1	2.54333	3.71056	2.36472	5.76623	2.85406
B5	24×12^3	1.125	3.11413	1.03624	0.533927	2.64676	1.60002
B6	24×12^3	1.15	1.51009	3.61068	0.122117	4.28713	0.420703
B7	24×12^3	1.175	3.05379	0.169209	0.492669	3.59039	0.854043
B8	24×12^3	1.18	1.84539	0.456036	0.226258	2.9395	1.20918
B9	24×12^3	1.185	1.71852	0.384545	1.35089	1.91835	1.48933
B10	24×12^3	1.19	1.74255	1.0647	0.897999	1.21423	1.90816

Table 16: Pull of wall-smearred results from local results on 24×12^3 lattice.

lattice	V	$-am_0$	am_{PS}^2/m	m_V/F_{PS}	m_V/m_{PS}	$a^3(m_{PS}F_{PS})^2/m$	F_V/F_{PS}
C0	32×16^3	1.15	1.93171	3.06861	0.882135	4.34396	1.47396
C1	32×16^3	1.175	1.06468	2.32532	0.137237	3.31804	0.411924
C2	32×16^3	1.18	2.03676	1.54644	0.0619247	3.39686	1.57362
C3	32×16^3	1.185	2.39644	0.563872	0.653246	1.82322	1.42152
C4	32×16^3	1.19	2.26197	0.559476	0.623971	2.59077	1.87611

Table 17: Pull of wall-smearred results from local results on 32×16^3 lattice.

lattice	V	$-am_0$	am_{PS}^2/m	m_V/F_{PS}	m_V/m_{PS}	$a^3(m_{PS}F_{PS})^2/m$	F_V/F_{PS}
D0	64×24^3	1.18	2.04515	3.80398	1.32766	3.07595	1.80012
D1	64×24^3	1.185	0.739296	3.8496	0.192169	2.02015	0.0468305
D2	64×24^3	1.19	0.139092	0.267849	0.156939	0.100296	0.348643

Table 18: Pull of wall-smearred results from local results on 64×24^3 lattice.

References

- [1] S. Weinberg, *Implications of Dynamical Symmetry Breaking*, *Phys. Rev.* **D13** (1976) 974–996.
- [2] L. Susskind, *Dynamics of Spontaneous Symmetry Breaking in the Weinberg- Salam Theory*, *Phys. Rev.* **D20** (1979) 2619–2625.
- [3] B. Holdom, *Technicolor*, *Phys. Lett.* **B150** (1985) 301.
- [4] K. Yamawaki, M. Bando, and K.-i. Matumoto, *Scale Invariant Technicolor Model and a Technidilaton*, *Phys. Rev. Lett.* **56** (1986) 1335.
- [5] T. W. Appelquist, D. Karabali, and L. C. R. Wijewardhana, *Chiral Hierarchies and the Flavor Changing Neutral Current Problem in Technicolor*, *Phys. Rev. Lett.* **57** (1986) 957.
- [6] M. A. Luty and T. Okui, *Conformal technicolor*, *JHEP* **09** (2006) 070, [[hep-ph/0409274](#)].
- [7] C. T. Hill and E. H. Simmons, *Strong dynamics and electroweak symmetry breaking*, *Phys. Rept.* **381** (2003) 235–402, [[hep-ph/0203079](#)].
- [8] F. Sannino, *Conformal Dynamics for TeV Physics and Cosmology*, *Acta Phys. Polon.* **B40** (2009) 3533–3743, [[arXiv:0911.0931](#)].
- [9] M. Piai, *Lectures on walking technicolor, holography and gauge/gravity dualities*, *Adv. High Energy Phys.* **2010** (4302) [[arXiv:1004.0176](#)].
- [10] C. Nunez, I. Papadimitriou, and M. Piai, *Walking Dynamics from String Duals*, *Int. J. Mod. Phys.* **A25** (2010) 2837–2865, [[arXiv:0812.3655](#)].
- [11] D. Elander, C. Nunez, and M. Piai, *A light scalar from walking solutions in gauge-string duality*, *Phys. Lett.* **B686** (2010) 64–67, [[arXiv:0908.2808](#)].
- [12] T. DeGrand, *Lattice studies of QCD-like theories with many fermionic degrees of freedom*, [arXiv:1010.4741](#).
- [13] L. Del Debbio, *The conformal window on the lattice*, *PoS LATTICE2010* (2010) 004.
- [14] D. D. Dietrich and F. Sannino, *Walking in the $SU(N)$* , *Phys. Rev.* **D75** (2007) 085018, [[hep-ph/0611341](#)].
- [15] A. J. Hietanen, K. Rummukainen, and K. Tuominen, *Evolution of the coupling constant in $SU(2)$ lattice gauge theory with two adjoint fermions*, *Phys. Rev.* **D80** (2009) 094504, [[arXiv:0904.0864](#)].
- [16] F. Bursa, L. Del Debbio, L. Keegan, C. Pica, and T. Pickup, *Mass anomalous dimension in $SU(2)$ with two adjoint fermions*, *Phys. Rev.* **D81** (2010) 014505, [[arXiv:0910.4535](#)].

- [17] T. DeGrand, Y. Shamir, and B. Svetitsky, *Infrared fixed point in $SU(2)$ gauge theory with adjoint fermions*, arXiv:1102.2843.
- [18] S. Catterall and F. Sannino, *Minimal walking on the lattice*, *Phys. Rev.* **D76** (2007) 034504, [arXiv:0705.1664].
- [19] L. Del Debbio, A. Patella, and C. Pica, *Higher representations on the lattice: numerical simulations. $SU(2)$ with adjoint fermions*, *Phys. Rev.* **D81** (2010) 094503, [arXiv:0805.2058].
- [20] S. Catterall, J. Giedt, F. Sannino, and J. Schneible, *Phase diagram of $SU(2)$ with 2 flavors of dynamical adjoint quarks*, *JHEP* **11** (2008) 009, [arXiv:0807.0792].
- [21] A. Hietanen, J. Rantaharju, K. Rummukainen, and K. Tuominen, *Minimal technicolor on the lattice*, *Nucl. Phys.* **A820** (2009) 191c–194c.
- [22] L. Del Debbio, B. Lucini, A. Patella, C. Pica, and A. Rago, *Conformal versus confining scenario in $SU(2)$ with adjoint fermions*, *Phys.Rev.* **D80** (2009) 074507, [arXiv:0907.3896].
- [23] S. Catterall, J. Giedt, F. Sannino, and J. Schneible, *Probes of nearly conformal behavior in lattice simulations of minimal walking technicolor*, arXiv:0910.4387.
- [24] L. Del Debbio, B. Lucini, A. Patella, C. Pica, and A. Rago, *The infrared dynamics of Minimal Walking Technicolor*, *Phys. Rev.* **D82** (2010) 014510, [arXiv:1004.3206].
- [25] L. Del Debbio, B. Lucini, A. Patella, C. Pica, and A. Rago, *Mesonic spectroscopy of Minimal Walking Technicolor*, *Phys.Rev.* **D82** (2010) 014509, [arXiv:1004.3197].
- [26] T. DeGrand and A. Hasenfratz, *Remarks on lattice gauge theories with infrared-attractive fixed points*, *Phys. Rev.* **D80** (2009) 034506, [arXiv:0906.1976].
- [27] B. Lucini, *Strongly Interacting Dynamics beyond the Standard Model on a Spacetime Lattice*, arXiv:0911.0020.
- [28] L. Del Debbio and R. Zwicky, *Scaling relations for the entire spectrum in mass-deformed conformal gauge theories*, arXiv:1009.2894.
- [29] L. Del Debbio and R. Zwicky, *Hyperscaling relations in mass-deformed conformal gauge theories*, *Phys. Rev.* **D82** (2010) 014502, [arXiv:1005.2371].
- [30] E. Kerrane *et. al.*, *Improved Spectroscopy of Minimal Walking Technicolor*, arXiv:1011.0607.
- [31] **SciDAC Collaboration, LHPC Collaboration, UKQCD Collaboration** Collaboration, R. G. Edwards and B. Joo, *The Chroma software system for lattice QCD*, *Nucl.Phys.Proc.Suppl.* **140** (2005) 832, [hep-lat/0409003].
- [32] N. Madras and A. D. Sokal, *The Pivot algorithm: a highly efficient Monte Carlo method for selfavoiding walk*, *J.Statist.Phys.* **50** (1988) 109–186.

- [33] T. A. DeGrand and R. D. Loft, *Wave function tests for lattice QCD spectroscopy*, *Comput.Phys.Commun.* **65** (1991) 84–91.
- [34] S. Elitzur, *Impossibility of Spontaneously Breaking Local Symmetries*, *Phys.Rev.* **D12** (1975) 3978–3982.
- [35] G. T. Fleming, S. D. Cohen, H.-W. Lin, and V. Pereyra, *Excited-State Effective Masses in Lattice QCD*, *Phys. Rev.* **D80** (2009) 074506, [[arXiv:0903.2314](https://arxiv.org/abs/0903.2314)].